PNAS

Supporting Information for

Article DOI: 10.1073/pnas.2310771121

Large enrichments in fatty acid $^{2}H/^{1}H$ ratios distinguish respiration from aerobic fermentation in yeast *Saccharomyces cerevisiae*

Ashley E. Maloney[a,b], Sebastian H. Kopf[b], Zhaoyue Zhang[c], Jamie McFarlin[d], Daniel B. Nelson[e], Andrew L. Masterson[f] , and Xinning Zhang[g]

[a]Department of Geosciences, Princeton University, Princeton, NJ 08544
[b]Department of Geological Sciences, University of Colorado Boulder, Boulder, CO 80309
[c]Lewis-Sigler Institute for Integrative Genomics and Department of Chemistry, Princeton University, Princeton, NJ 08544
[d]Department of Geology and Geophysics, University of Wyoming, Laramie, WY 82071
[e]Department of Environmental Science— Botany, University of Basel, Basel 4056, Switzerland
[f]Department of Earth and Planetary Sciences, Northwestern University, Evanston, IL 60208
[g]High Meadow Environmental Institute and Department of Geosciences, Princeton University, Princeton, NJ 08544

Email: A. E. Maloney (ashley.maloney@colorado.edu), X. Zhang (xinningz@princeton.edu)

This PDF file includes:

SI Figures:

- **Fig. S1**. Detailed accounting of NADPH-related hydrogen flows in central metabolism of yeast *Saccharomyces cerevisiae.*
- **Fig. S2**. *S. cerevisiae* $\delta^{2}H$ values for lipid, water, and substrate, and lipid-water and lipid-substrate ^{2}H-fractionations across substrates and dilution rates.
- **Fig. S3**. Fatty acid, growth water, and substrate $\delta^{2}H$ values.
- **Fig. S4**. Cellular redox cofactor ratios of strain EXF-4126 grown in chemostats.
- **Fig. S5**. Extracellular ethanol levels and ammonium levels in medium.
- **Fig. S6**. Relative contributions of $NADP^{+}$-reducing enzymes to total NADPH production.
- **Fig. S7**. Relative enzyme activities in glycerol-respiration vs glucose-fermentation.
- **Fig. S8**. Biomass composition of *S. cerevisiae* across growth rates and substrates.
- **Fig. S9**. Statistical analyses of relationships between EXF-4126 fatty acid ^{2}H-fractionations and various physiological parameters.
- **Fig. S10**. Model of fatty acid ^{2}H-fractionation relationship with weight abundance lipids in glucose-grown yeast biomass.
- **Fig. S11**. Statistical analyses of relationships between EXF-4126 ^{2}H-fractionations between palmitoleic (n-$C_{16:1}$) and palmitic (n-$C_{16:0}$) fatty acids and various physiological parameters.
- **Fig. S12**. Palmitic (n-$C_{16:0}$) and palmitoleic (n-$C_{16:1}$) acid ^{2}H-fractionation values of yeast and other cultured organisms.
- **Fig. S13**. Bulk biomass elemental analysis and isotope ratios vs growth rate: biomass/substrate ^{13}C isotope fractionation, biomass/ammonium ^{15}N isotope fractionation, and C/N ratios.
- **Fig. S14**. Biosynthetic ^{2}H-fractionation vs growth rate for yeast and other organisms.

Table S1. Deuterium kinetic isotope effects (dKIEs) of NAPDH-producing enzymes.

Table S2. Statistical analyses of EXF-4126 fatty acid/water ^{2}H-fractionations and various physiological parameters.
SI Methods 1–5
SI Discussion 1–6
SI References

Other supporting materials for this manuscript include the following:
Data S1–S4 (separate files)

Data S1. "Data_S1_all_data.xls" Strain EXF-4126 glycerol and glucose chemostat datasets: tabs include growth_rates: chemostat growth rates [*growth_rate.1_d* (growth rate in d^{-1})],
lipids_all: lipid abundances and hydrogen isotope fractionations [*ab.ug_mg* (relative abundance fatty acid in biomass µg fatty acids mg dried biomass^{-1}); *recovery* (% recovery), *eps_fa_water.permil* (average fatty acid ^{2}H-fractionations in ‰); *eps_fa_water_sd.permil* (SD average fatty acid ^{2}H-fractionations in ‰)],
enzymes_all: Enzyme NADPH production rates for $NADP^{+}$-reducing enzymes [enzymes include *g6p* (Glucose-6-Phosphate Dehydrogenase), *6pg* (6-Phosphogluconate Dehydrogenase), *ALDH* (Aldehyde Dehydrogenase), *IDH* (Isocitrate Dehydrogenase); *rate* (enzyme activity in mol NADPH mg total protein^{-1} min^{-1}],
bulk_all: biomass elemental and isotopic composition [*CN* (biomass C/N ratios); *d15N* (biomass N stable isotopic composition δ^{15}N ‰); *substrate_d15N* (substrate N stable isotopic composition δ^{15}N ‰); *SD_substrate_d15N* (SD substrate N stable isotopic composition δ^{15}N ‰); *d13C* (biomass C stable isotopic composition δ^{13}C ‰); *substrate_d13C* (substrate C stable isotopic composition δ^{13}C ‰); *SD_substrate_d13C* (SD substrate C stable isotopic composition δ^{13}C ‰)].

Data S2. "Data_S2_data_summary.xls" Average and standard deviations of enzyme NADPH production rates (g6p, 6pg, ALDH, IDH as total IDH and cytosolic IDH in mol NADPH mg total protein^{-1} min^{-1}), proportional contributions of enzymes to NAPDH production (%), relative abundance lipids in biomass (µg fatty acids mg dried biomass^{-1}), fatty acid ^{2}H-fractionations (‰), biomass composition [*CN*, biomass C/N ratios, *d15N*, biomass N stable isotopic composition (δ^{15}N ‰), *d13C*, biomass C stable isotopic composition (δ^{13}C ‰)].

Data S3. "Data_S3_stats.xls" Pearson r and p_{val}, York linear regression (york p_{val}) for all glycerol and glucose chemostat data, glycerol only, and glucose only data sets.
Notation:
all_eps.permil (fatty acid average ^{2}H-fractionations $^{2}\varepsilon_{fattyacid/water}$ in ‰),
growth_rate.1_d (growth rate in d^{-1}),
% cyto IDH (% cytosolic IDH to NAPDH),
% total IDH (% mitochondrial + cytosolic IDH to NAPDH),
CN (biomass C/N ratios),
% unsat (% fatty acids of total fatty acids recovered),
all_ab.ug_mg (fatty acid relative abundance in biomass, microgram fatty acids mg dry biomass^{-1}),
1/all_ab.ug_mg (mg dry biomass microgram fatty acids^{-1}),
C16:1/C16:0_eps.permil (average ^{2}H-fractionation between palmitoleic and palmitic fatty acids, $^{2}\varepsilon_{16:1/16:0}$ in ‰)

Data S4. "Data_S4_rawdata.xls" Chemostat raw data feeding into Data S1: tabs include growth rates, lipid isotopes (d2H_water and d2H_fatty acids), lipid abundances (EXF-4126 only), enzyme raw data (rates Vm, total protein BCA concentrations, EXF-4126 only), bulk compositions (biomass C/N ratios, d15N, d13C), NAD(P)(H) (EXF-4126 only), supernatant ethanol, supernatant ammonia.

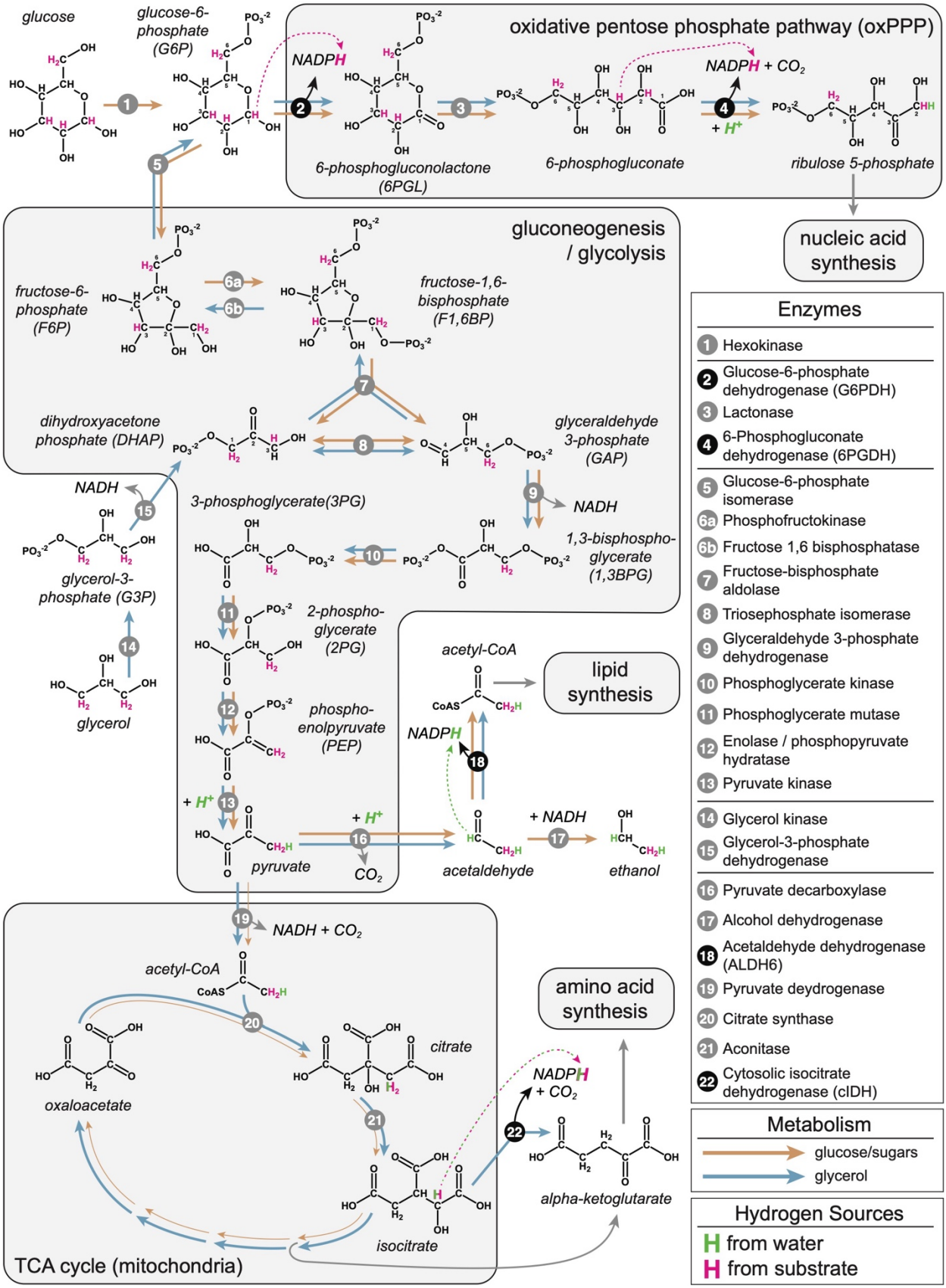

Fig. S1. Detailed accounting of NADPH-related hydrogen flows in yeast *Saccharomyces cerevisiae* for glycerol respiration and aerobic fermentation of sugars. Not shown: In ethanol-producing yeast, NADPH hydrogen can come indirectly from NADH when ethanol is reassimilated (1). Sugar rearrangements (C3-C6) are fast, reversible, and thus express equilibrium isotope effects (see **SI Discussion 1**), isotope effects for other reactions are expected to be kinetic.

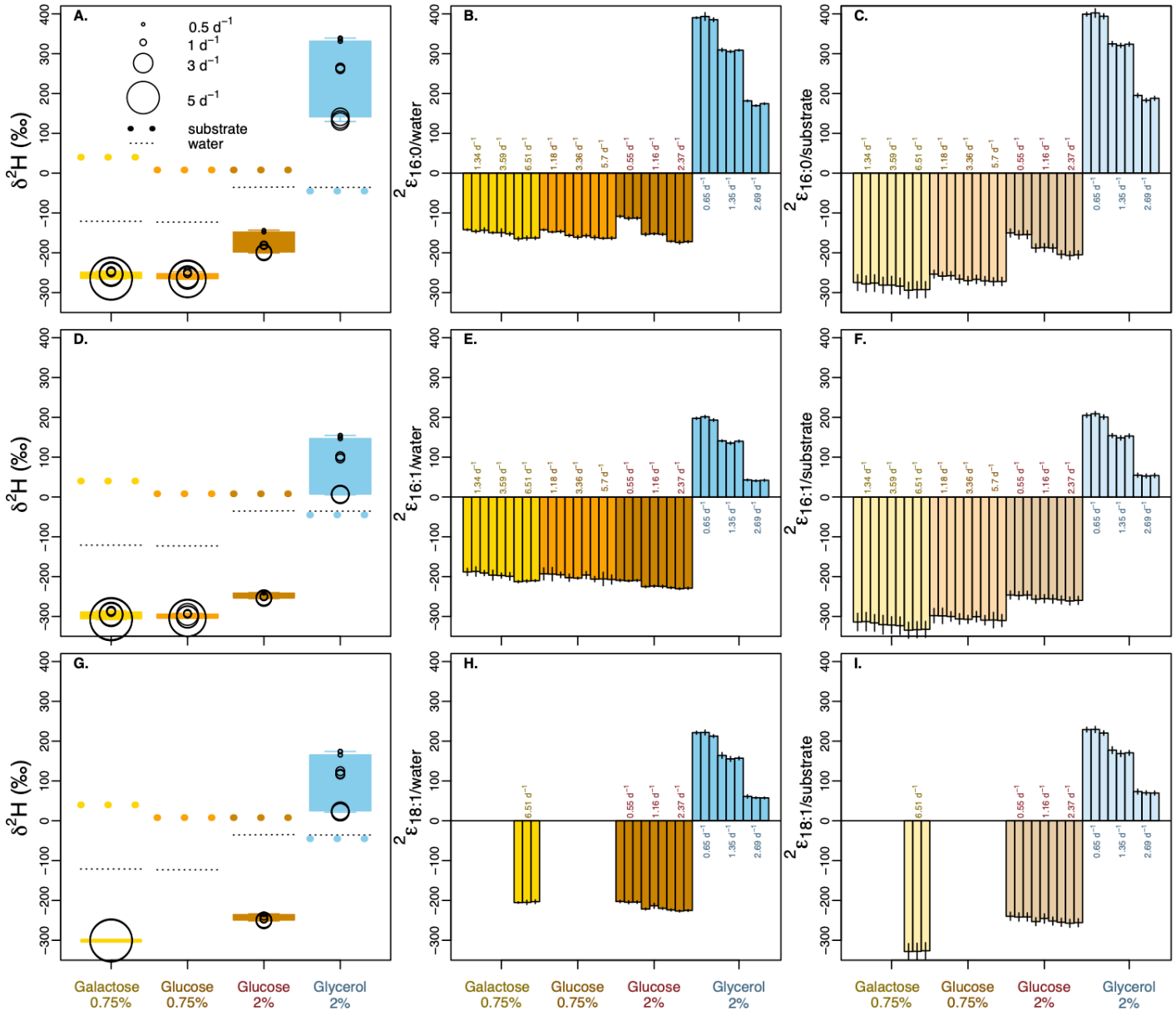

Fig. S2. *S. cerevisiae* δ^2H values for lipid, water, and substrate, and lipid/water and lipid/substrate ^2H-fractionations across substrates and dilution rates. A, D, G): δ^2H values of palmitic, palmitoleic, and oleic fatty acids (shaded boxes with black circles sized relative to the dilution rate; three samples per rate); δ^2H values of growth water (thin black dotted horizontal bars); δ^2H values of substrates glycerol (−45 ± 5‰), glucose (8 ± 10‰), and galactose (40 ± 20‰) as thick dotted horizontal bars. The shift in growth water (and therefore lipid) δ^2H values is due to location: δ^2H water in Boulder CO (~ −120‰) and Princeton NJ (~ −35‰). B, E, H): the hydrogen isotope lipid-water fractionation between palmitic, palmitoleic, and oleic fatty acids and growth water for each substrate and growth rate. C, F, I): the hydrogen isotope lipid-substrate fractionation between palmitic, palmitoleic, and oleic fatty acids and carbon substrate for each substrate and growth rate; error bars are propagated errors of δ^2H_{water} or $\delta^2H_{substrate}$ analytical uncertainty and standard deviation of three IRMS injections, the difference of two injections, or the mean error of this sample set (6‰) if only one injection; dilution rates are indicated outside each set of three bars. Strain FY4 grown with 0.75% glucose (orange), 0.75% galactose (gold); strain EXF-4126 grown with 2% glycerol (blue), 2% glucose (brown) (**Data S1, S4**).

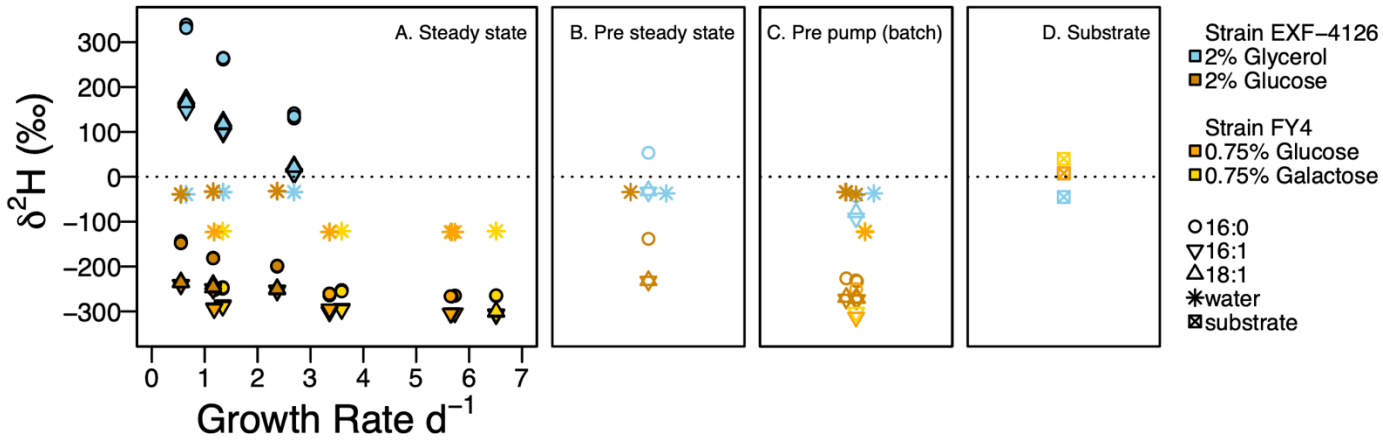

Fig. S3. **Fatty acid, growth water, and substrate δ^2H values.** A) Sample δ^2H values in steady state chemostat conditions under controlled growth rates; filled symbols for fatty acids. B) Pre steady state samples (uncontrolled growth rate), unfilled symbols for fatty acids. C) Pre-pump samples in late exponential/early stationary taken from the bioreactor just prior to turning on pumps and initiating chemostats (uncontrolled growth rate), unfilled symbols for fatty acids. D) Carbon substrate δ^2H values. Strain EXF-4126 grown with 2% glycerol (blue), 2% glucose (brown); strain FY4 grown with 0.75% glucose (gold), 0.75% galactose (orange) (**Data S4**).

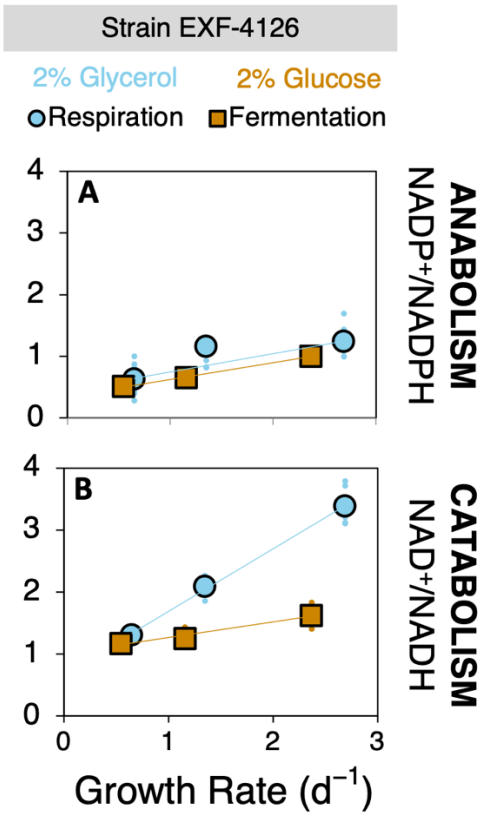

Fig. S4. Cellular redox status. A) anabolic redox cofactor poise $NADP^+$/NADPH and B) catabolic redox cofactor poise NAD^+/NADH versus growth rate in chemostats of strain EXF-4126 (**Data S4**). Large blue circles (glycerol-respiration) and brown squares (glucose-fermentation) represent the mean of 4 to 6 sample time points at each growth rate (small dots).

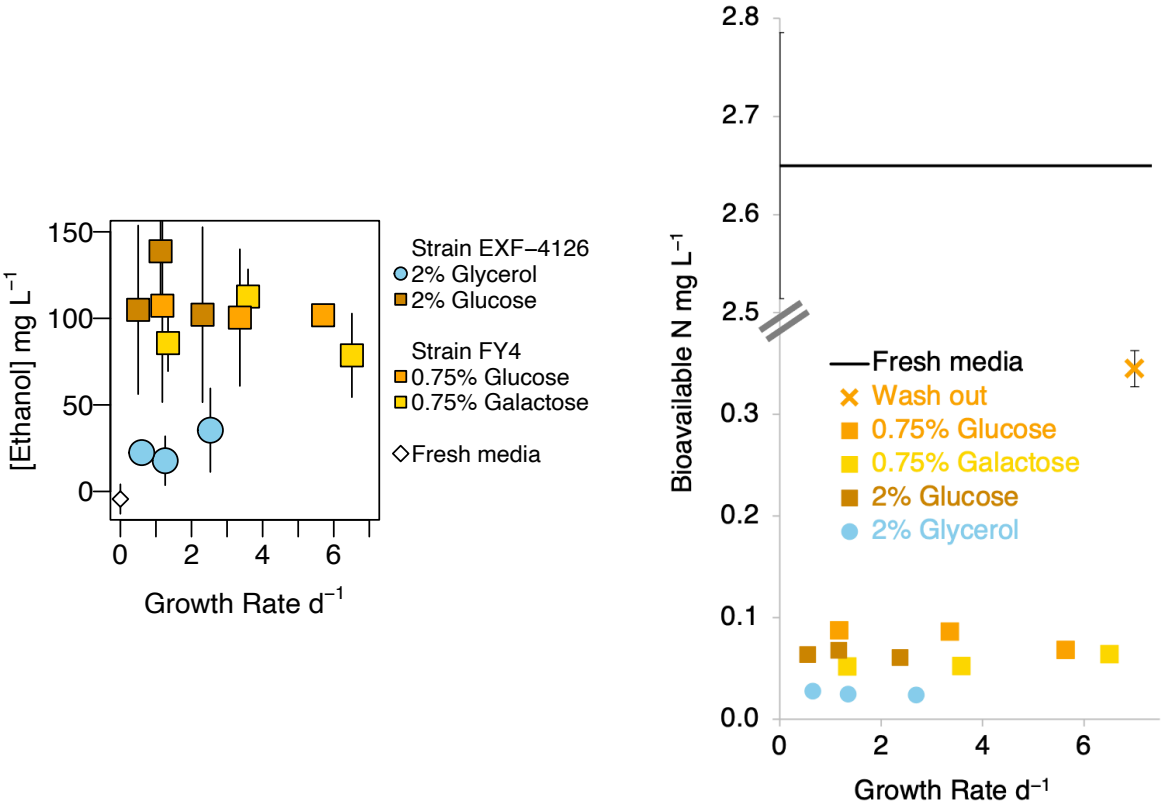

Fig. S5. Extracellular ethanol levels (left panel) and ammonium levels in growth medium (right panel). LEFT: Higher levels of fermentation overflow product ethanol confirm much higher fermentation in glucose and galactose cultures compared to glycerol cultures. Error bars are SD of triplicate sampling timepoints. Ethanol in fresh media was below the 0.1 mg L^{-1} detection limit. RIGHT: Ammonium levels in chemostat media during stable growth on sugars and glycerol were barely detectable (< ~0.1 mg L^{-1}; detection limit = 0.017 mg L^{-1}) and much lower than in washout conditions when pump rate was faster than the fastest growth rate (~0.35 mg L^{-1}, only sampled for the 0.75% glucose condition) and far lower than fresh media (black horizontal line, 2.65 mg L^{-1}). This indicates N-limitation in chemostats yielded steady state N limited growth at relevant growth rates. Error bars are the difference between two measurements (fresh media) or 5% of absolute value (culture supernatant, not visible on most data points); note break in y-axis. Strain EXF-4126 (2% glucose (brown squares) and glycerol (blue circles)), strain FY4 (0.75% galactose (gold squares) and glucose (orange squares)) (**Data S4**).

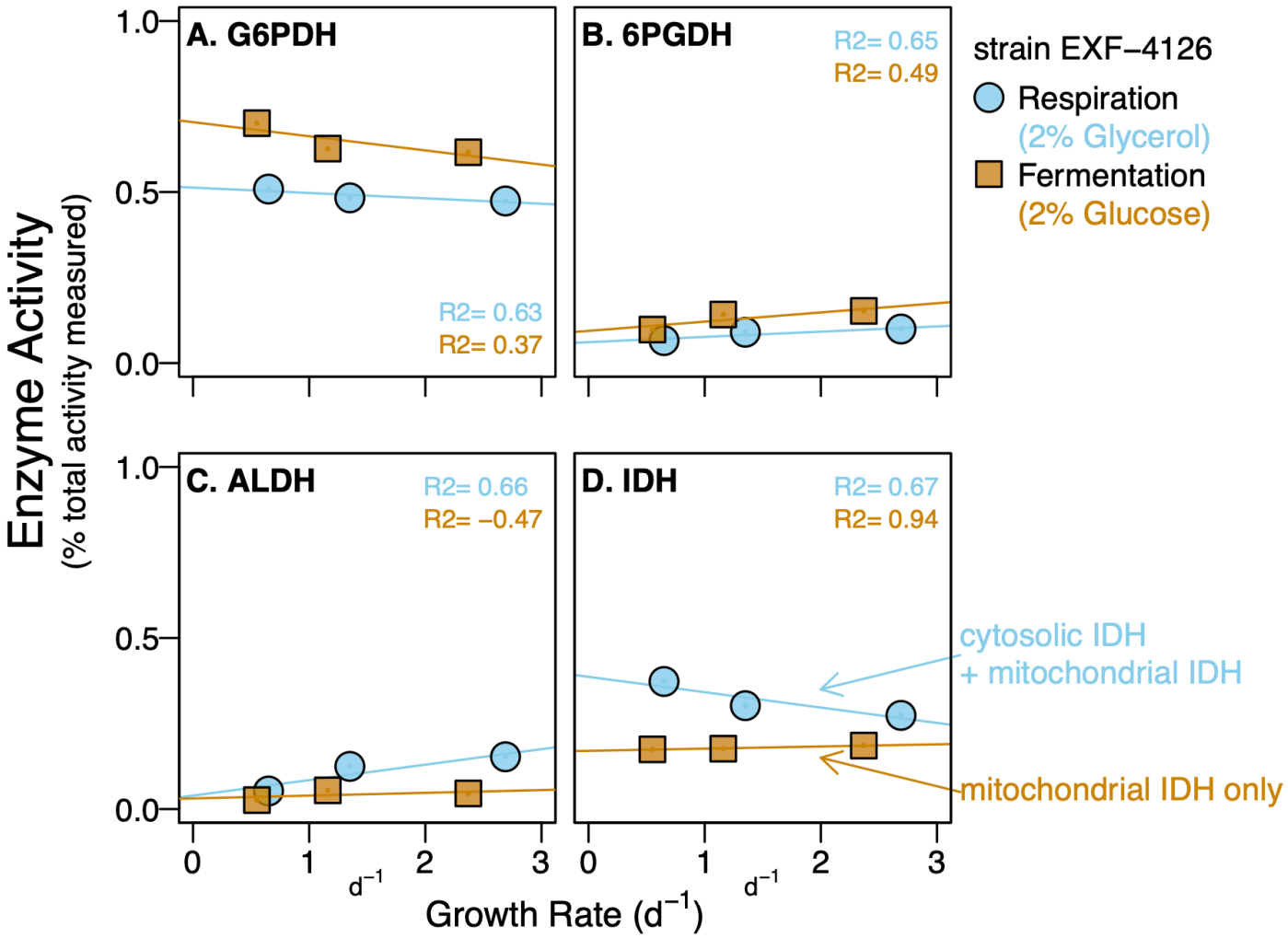

Fig. S6. Relative contributions of NADP$^+$-reducing enzymes to total NADPH production activity based on measured enzyme activities. Glycerol-respiring (blue circles) and glucose-fermenting (brown squares) chemostats of strain EXF-4126. Measured IDH activity for glucose-grown cells is assumed to represent mitochondrial IDH as the cytosolic form is glucose repressed (**Fig. 3, Data S1, S2, S4**).

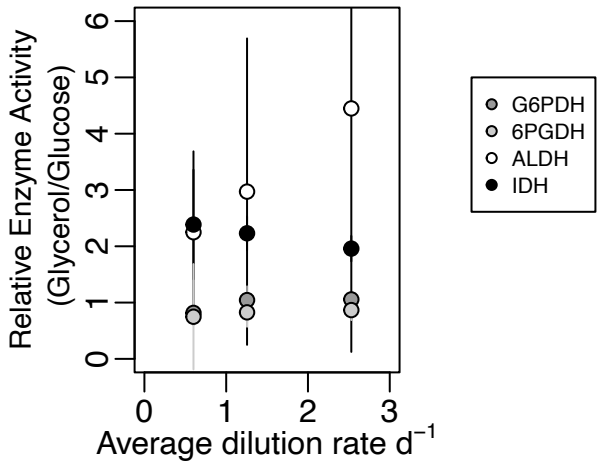

Fig. S7. **Relative activities of different NADP$^+$-reducing enzymes in glycerol-respiration vs glucose-fermentation.** Since glucose and glycerol had slightly different growth rates, the average growth rate is used here to show relative enzyme activities, strain EXF-4126 only. Error bars indicate standard deviation of 4 to 11 separate time points taken during each growth rate (**Fig 3, Data S1, S2, S4**).

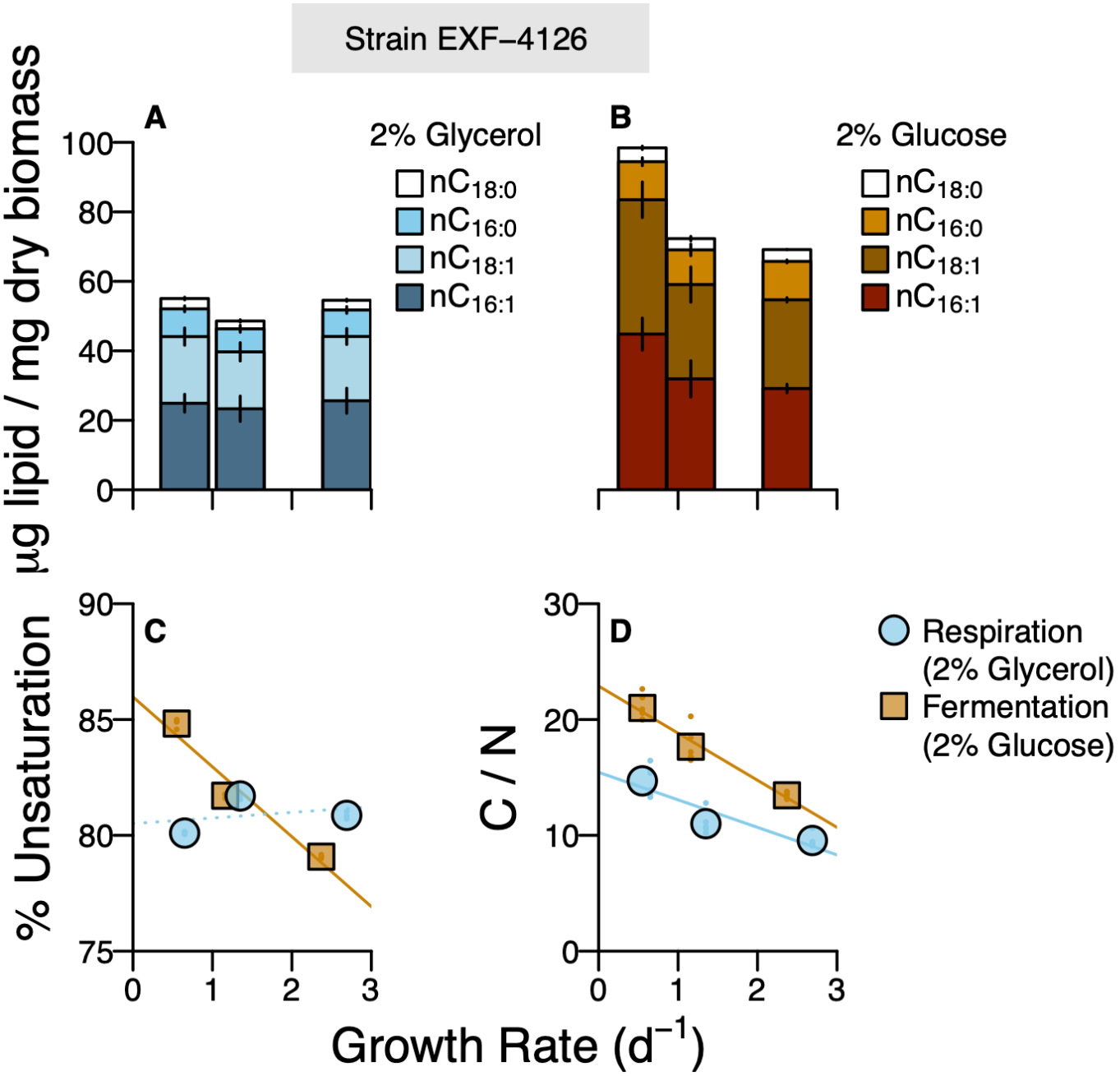

Fig. S8. Biomass composition of *S. cerevisiae* EXF-4126 across growth rates and substrates. Relative abundances of major fatty acids in biomass in A) glycerol-fed fermenting and B) glucose-fed respiring chemostats; error bars are SD of 3 steady state replicate timepoints. C) Percent unsaturation of fatty acids. D) Biomass C/N ratios, 3 to 6 sample replicates**.** Solid lines indicate linear regressions ($p < 0.001$) (**Data S1**–**S4**).

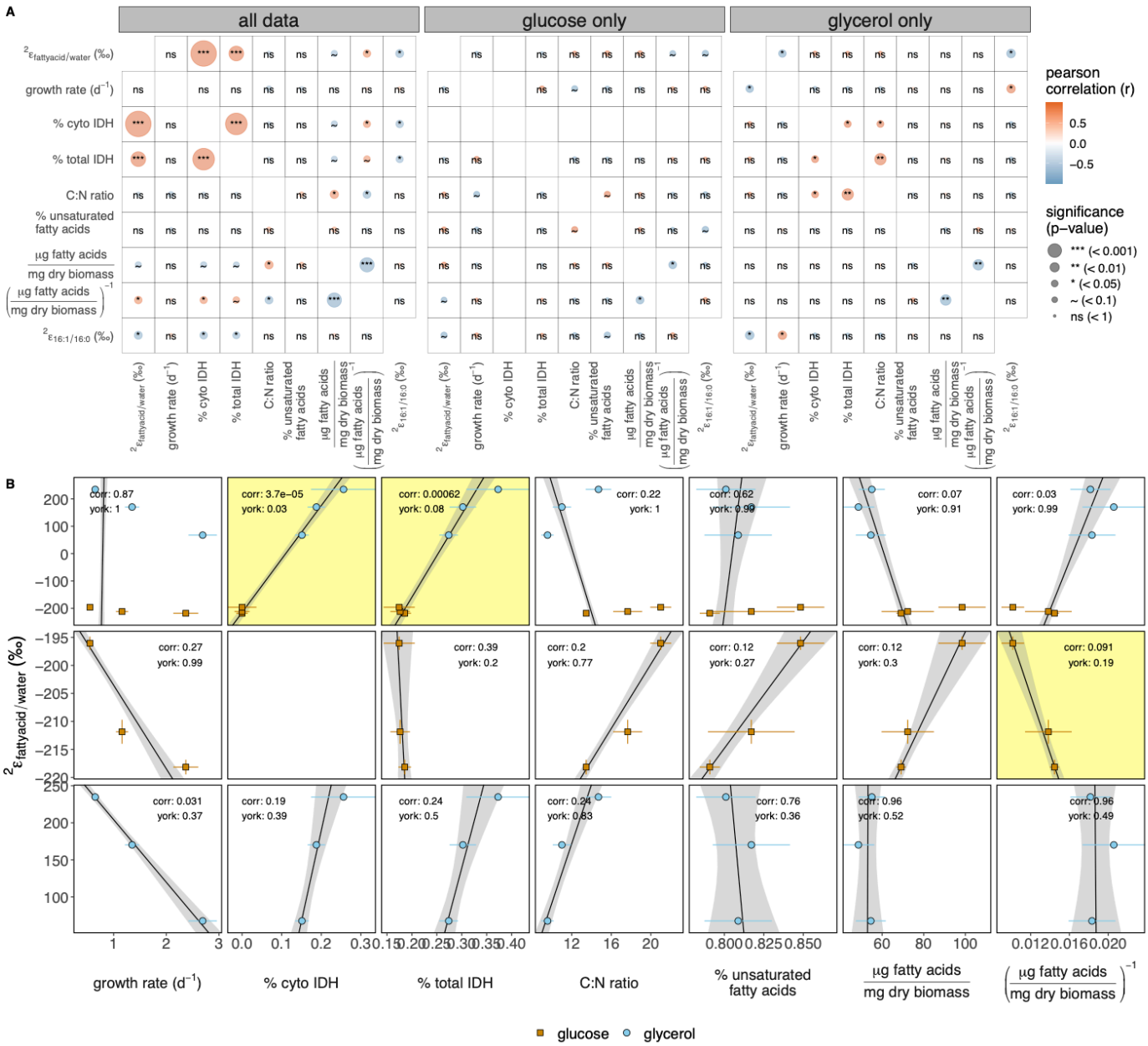

Fig. S9. Statistical analyses of relationships between EXF-4126 fatty acid ^{2}H-fractionations and various physiological parameters. A) Pearson correlations (r) and p-values. B) 95% confidence intervals for York linear regressions. Yellow highlight for significant correlations with Pearson correlation (corr) < 0.1, York linear correlation (York) pval < 0.2. Note, calculations of relative contributions to NADPH based on protein activity data assume 1) similar protein extraction efficiencies and for cytosolic IDH 2) only mitochondrial IDH is active for glucose metabolism such that the cytosolic contribution (% cyto IDH) in glycerol metabolism is estimated by correcting for the estimated mitochondrial component. See **Data S1**–**S4** for details.

$$f = L \cdot \frac{m_{lipids}}{m_{cell}} = L \cdot ab_{all}$$

$$\begin{aligned} R_{cell} &= f \cdot R_{lipids} + (1-f) \cdot R_{other} \\ &= f \cdot R_{lipids} + (1-f) \cdot \alpha_{o/l} \cdot R_{lipids} \end{aligned}$$

$$\rightarrow R_{lipids} = \frac{R_{cell}}{f + (1-f) \cdot \alpha_{o/l}} = \frac{R_{cell}}{f \cdot (1-\alpha_{o/l}) + \alpha_{o/l}}$$

$$\rightarrow \epsilon_{lipids/water} + 1 = \frac{\epsilon_{cell/water} + 1}{L \cdot ab_{all} \cdot (1-\alpha_{o/l}) + \alpha_{o/l}}$$

$$\approx \epsilon_{lipids/water} \propto \frac{1}{ab_{all}}$$

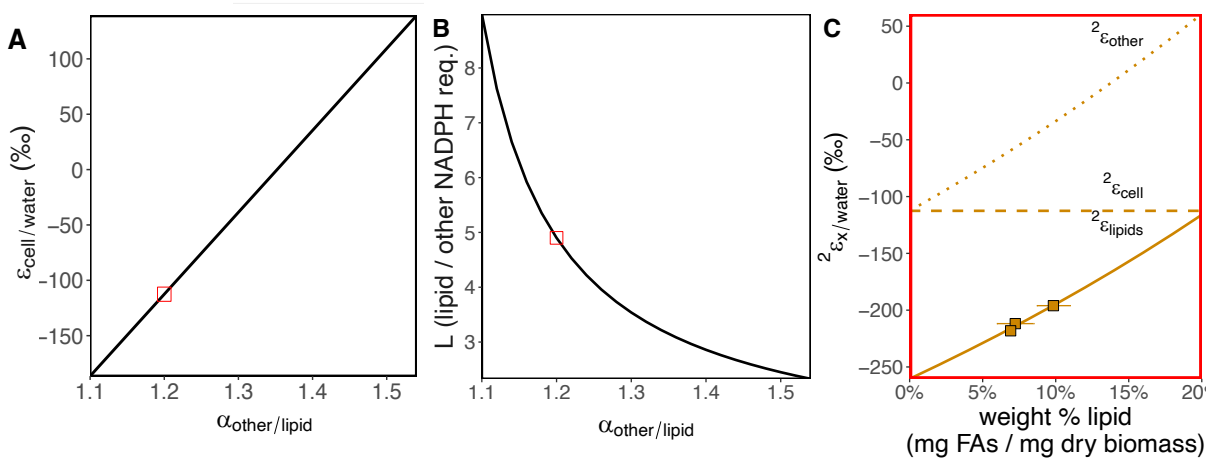

Fig. S10. Isotopic model of lipid/water ^{2}H-fractionation relationship with weight abundance fatty acids in glucose-grown yeast biomass (top panel) predicts a linear relationship between $^2\varepsilon_{lipid/water}$ and the reciprocal of lipid weight abundances in biomass. Assuming that ^{2}H isotopes in bulk cells and constituents are only driven by NADPH cycling, an isotope mass balance between ^{2}H isotopes in cells (R_{cell}) and in lipids (R_{lipid}) can be derived based on variable partitioning between NAPDH to lipids and non-lipid constituents (f), which results from cellular lipid abundance and the relatively higher NADPH demands of lipid biosynthesis vs other biomass constituents (L), and the fractionation factor between other biomass constituents and lipids ($^2\alpha_{other/lipid}$), which sets the isotopic composition of non-lipid constituents relative to lipids. Rewritten, lipid/water ^{2}H-fractionation is thus set by cell/water ^{2}H-fractionation ($^2\varepsilon_{cell/water}$), the fraction of cellular NAPDH pool used for lipid biosynthesis (f = L*cellular lipid abundance), and non-lipid/lipid ^{2}H fractionation ($^2\alpha_{other/lipid}$). Boxes A–C highlight one example solution of $^2\varepsilon_{cell/water}$, $^2\alpha_{other/lipid,}$ and L that fit the measured lipid/water ^{2}H-fractionation and cellular lipid abundance values, indicating that observed ^{2}H depletions in glucose culture $^2\varepsilon_{lipid/water}$ values with faster growth rate and decreased cellular lipid content (main text **Fig. 4**) can be explained by changes in NAPDH demand resulting from cellular remodeling of lipids (solid line, lipid/water ^{2}H-fractionation, offset from dotted line, other/water ^{2}H-fractionation, by constant value set by $^2\alpha_{other/lipid}$, note ^{2}H repartitioning between lipids based on cell lipid abundance variations do not affect bulk cell/water ^{2}H, Box C). Isotopic mass balance model: ab_{all} (measured lipid weight abundance biomass); other (other biomass constituents); m_x (mass of cellular constituent x); f (fractional demand of total NADPH due to lipids biosynthesis); L (relative NADPH biosynthetic demand of lipids vs other materials); R_x (D/H of cellular constituent x); $^2\varepsilon_{cell/water}$ (fractionation of cell biomass relative to water driven solely by NADPH cycling), $^2\alpha_{other/lipid}$ (fractionation factor between other biomass constituents and lipids). The model assumes constant $^2\alpha_{other/lipid}$, $^2\varepsilon_{cell/water}$, and L values.

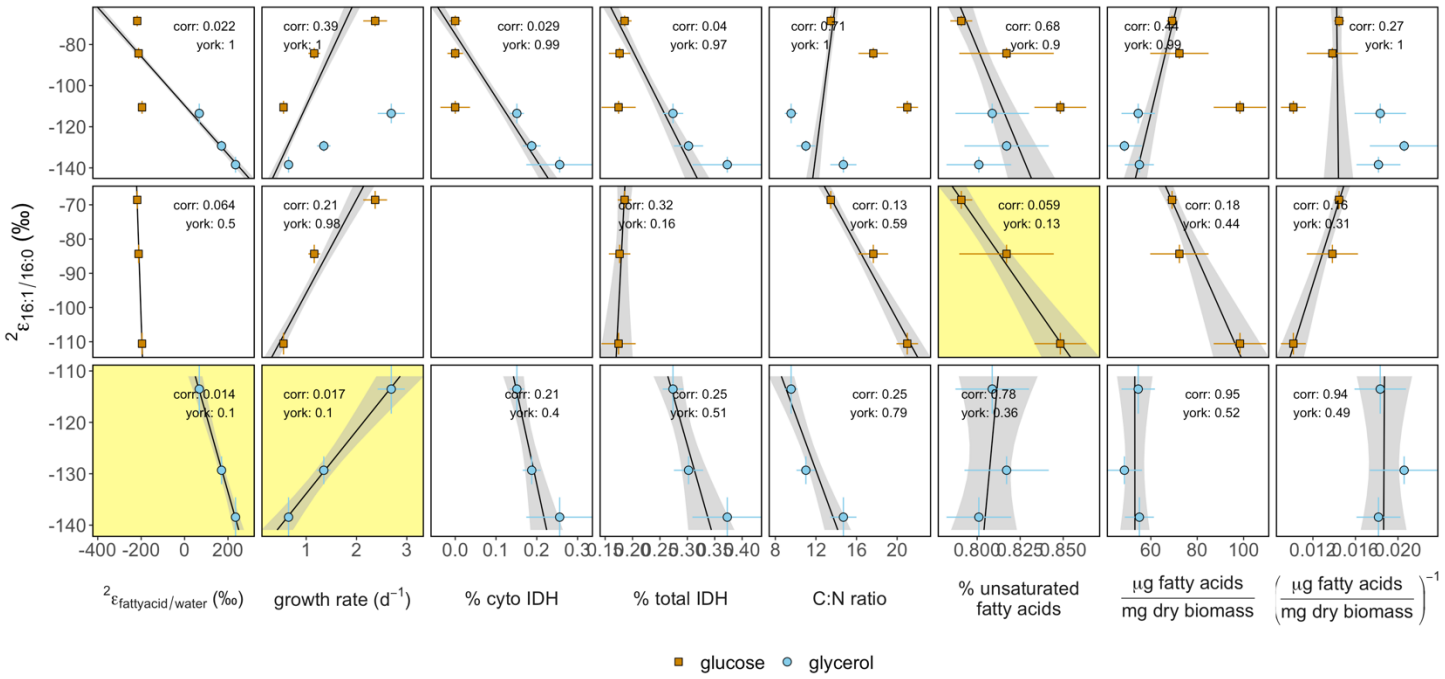

Fig. S11. Statistical analyses of relationships between EXF-4126 ^{2}H-fractionations between palmitoleic (16:1) and palmitic (16:0) fatty acids and various physiological parameters. 95% confidence intervals for York linear regressions. Yellow highlight for significant correlations with Pearson correlation (corr) < 0.1, York linear correlation (York) pval < 0.2 (2). See **Data S1**–**S3** for details.

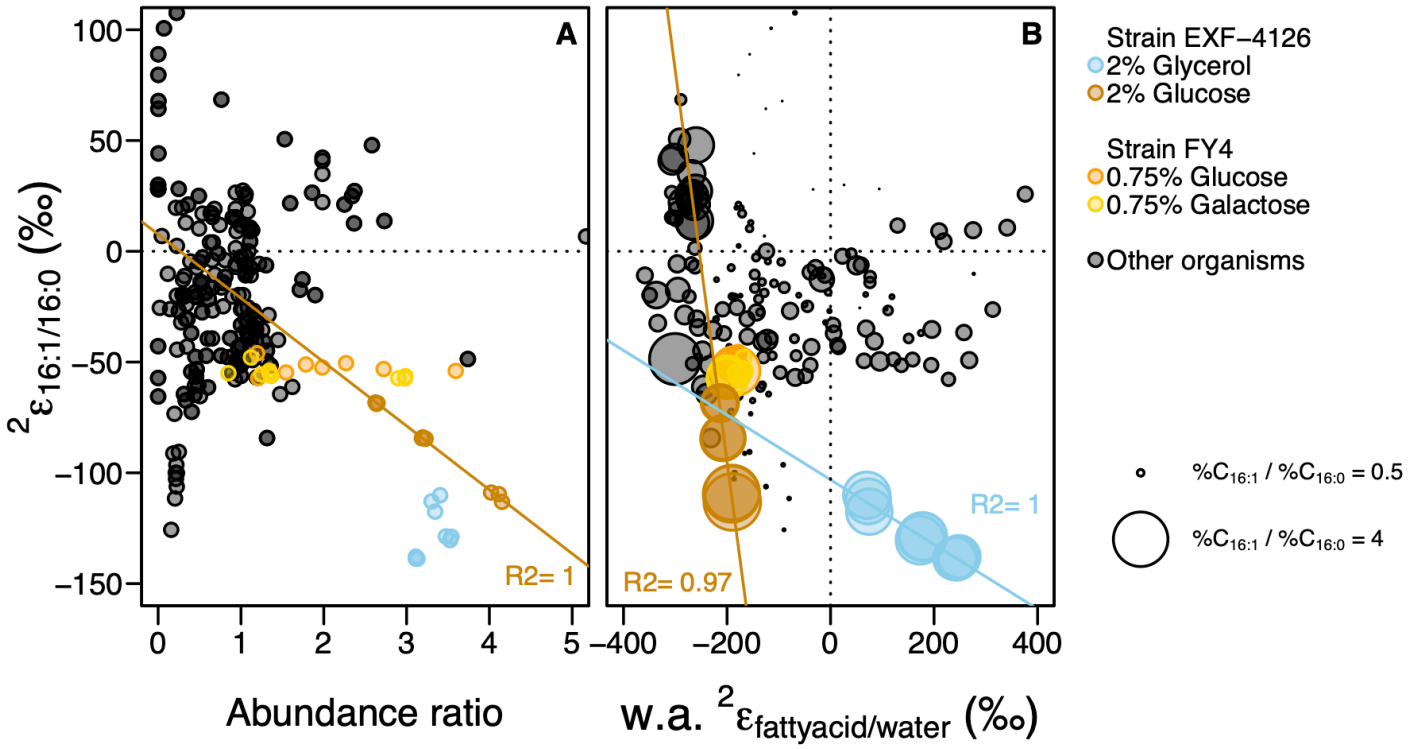

Fig. S12. Palmitic (*n*-$C_{16:0}$) and palmitoleic (*n*-$C_{16:1}$) acid ^{2}H-fractionation values ($^2\varepsilon_{16:1/16:0}$) of yeast and other cultured organisms. A) abundance ratio (% palmitoleic acid / % palmitic acid) and B) weighted averages (w.a.) of palmitoleic and palmitic acids $^2\varepsilon_{fattyacid/water}$. Chemostats of strain EXF-4126 fed glycerol (blue) or glucose (brown); strain FY4 fed glucose (orange) or galactose (yellow); and other cultured autotrophs (3–8) and heterotrophs (5, 6, 9–13) (black). In panel B only, circle size represents relative abundance of 16 chain fatty acids. For yeast data all data points are shown but linear regressions use means of three timepoints at each growth rate; adjusted R^2 shown.

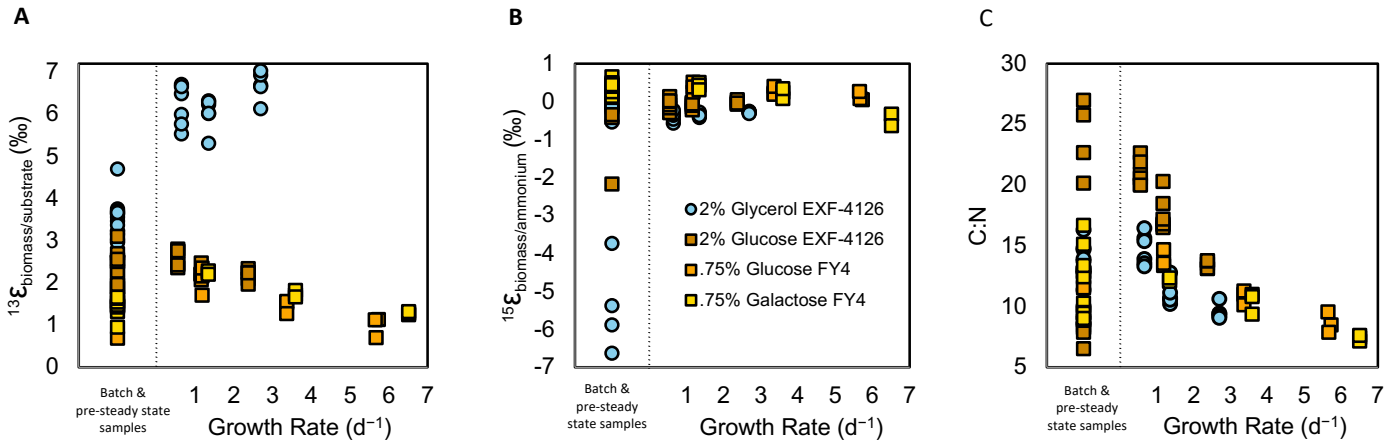

Fig. S13. Bulk biomass elemental and isotopic composition. A) Biomass/substrate ^{13}C isotope fractionation $^{13}\varepsilon_{biomass/substrate}$; B) biomass/ammonium ^{15}N isotope fractionation; C) C/N ratios. Strain EXF-4126 grown with 2% glycerol (blue circles), 2% glucose (brown squares); strain FY4 grown with 0.75% glucose (orange squares), 0.75% galactose (gold squares). Each data point is one of three to six time points sampled during steady state conditions at each growth rate, or (on the left of each panel) during batch cultures in flasks, bioreactor pre-pump batch conditions, or post-pump non steady state conditions (**Data S4**).

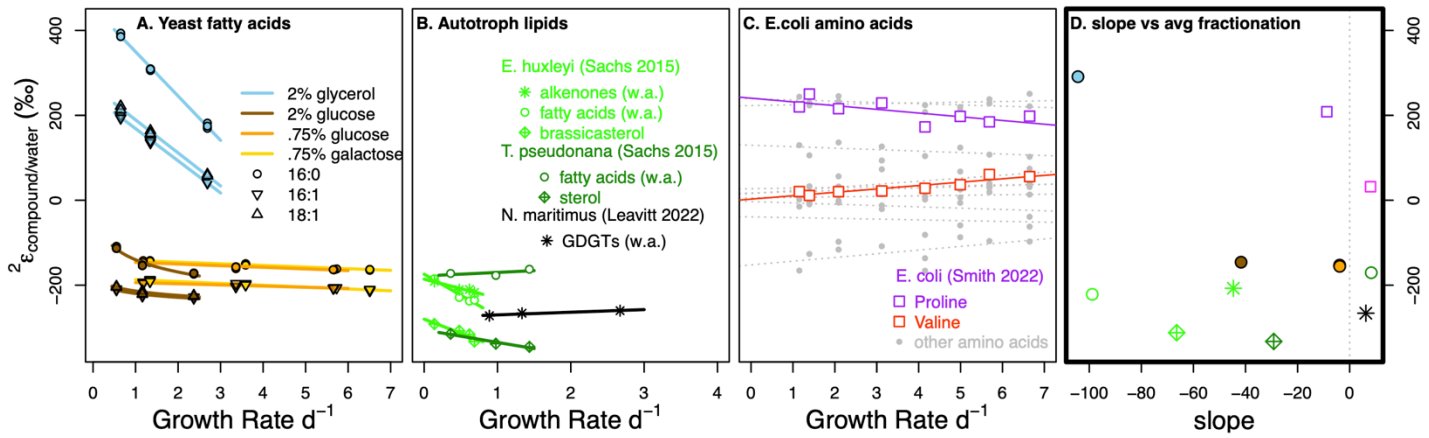

Fig. S14. Compound/water ^{2}H-fractionation versus growth rate for yeast and other organisms. A) Lipid/water ^{2}H-fractionation vs growth rate for *S. cerevisiae* fatty acids from cells grown on glycerol (blue), glucose (brown and orange), or galactose (gold) ($p < 0.01$, n=9). B) Lipid/water ^{2}H-fractionation vs growth rate for lipids from photoautotrophs *Thalassiosira pseudonana* and *Emiliania huxleyi* where individual alkenones and fatty acids are represented as the weighted average (w.a.) (4) with archaea lipids from (14) (note different horizontal scale). C) Amino acid/water ^{2}H-fractionation vs growth rate for individual amino acids from chemostat-grown bacteria *Escherichia coli* on glucose (15), proline and valine are highlighted in color to indicate they had a statistically significant relationship to growth rate. D) A summary of slopes and mean fractionation factors from A–C.

Table S1. **Deuterium kinetic isotope effects (dKIEs) of NAPDH-producing enzymes**. Experimental observations of the dKIE for $NADP^+$ reducing enzymes glucose 6-phosphate dehydrogenase (G6PDH), 6-phosphogluconate dehydrogenase (6PGDH), isocitrate dehydrogenase (IDH), and aldehyde dehydrogenase (ALDH). All experiments were performed at 25 °C, saturating $NADP^+$, and substrate concentrations were varied unless noted otherwise.

Enzyme	Organism	Substrates	Co-factor, Metal ion	pH	KIE [a]	$^2\varepsilon$ [b] (‰)	Reference
G6PDH	*Leuconostoc mesenteroides* (Sigma)	glucose 6-phosphate & [1-^{2}H]glucose 6-phosphate	$NADP^+$, Mg^{2+}	8	2.97	−663	Hermes et al., 1982 (16)
6PGDH	Yeast (Sigma)	6-phosphogluconate & [3-^{2}H]6-phosphogluconate	$NADP^+$, Mg^{2+}	5.05	2.54± 0.06	−606	Rendina et al., 1984 (17)
6PGDH	Yeast (Sigma)	6-phosphogluconate & [3-^{2}H]6-phosphogluconate	$NADP^+$, Mg^{2+}	5.94	2.11 ± 0.07	−526	Rendina et al., 1984 (17)
6PGDH	Yeast (Sigma)	6-phosphogluconate & [3-^{2}H]6-phosphogluconate	$NADP^+$, Mg^{2+}	7.34	1.93 ± 0.05	−482	Rendina et al., 1984 (17)
6PGDH	Yeast (Sigma)	6-phosphogluconate & [3-^{2}H]6-phosphogluconate	$NADP^+$, Mg^{2+}	8.0	1.54 ± 0.02	−351	Rendina et al., 1984 (17)
6PGDH	Yeast (Boehringer-Mannheim)	6-phosphogluconate & [3-^{2}H]6-phosphogluconate	$NADP^+$, Mg^{2+}	8.0	1.61 ± 0.04	−379	Rendina et al., 1984 (17)
6PGDH	Yeast (Sigma)	(saturating) 6-phosphogluconate & [3-^{2}H]6-phosphogluconate	$NADP^+$(variable), Mg^{2+}	8.0	1.77 ± 0.04	−435	Rendina et al., 1984 (17)
6PGDH	Yeast (Sigma)	6-phosphogluconate & [3-^{2}H]6-phosphogluconate	$NADP^+$, Mg^{2+}	9.10	1.37 ± 0.02	−270	Rendina et al., 1984 (17)
IDH	Pig heart (Sigma)	isocitrate & [2-^{2}H]isocitrate	$NADP^+$, Mg^{2+}	4.98	1.06 ± 0.03	−57	Grissom and Cleland, 1988 (18)
IDH	Pig heart (Sigma)	isocitrate & [2-^{2}H]isocitrate	$NADP^+$, Mg^{2+}	7	1	0	Grissom and Cleland, 1988 (18)
IDH	Not reported	isocitrate & [2-^{2}H]isocitrate	$NADP^+$, Mg^{2+}	4.5	1.08 ± 0.02	−74	Cook and Cleland, 1981 (19)
IDH	Not reported	isocitrate & [2-^{2}H]isocitrate	$NADP^+$, Mg^{2+}	7.5	1.07 ± 0.16 0.99 ± 0.09	−65 +10	Cook and Cleland, 1981; O'Leary, 1989 (19, 20)
IDH	Not reported	isocitrate & [2-^{2}H]isocitrate	$NADP^+$, Mg^{2+}	9.5	1.063 ± 0.008	−59	Cook and Cleland, 1981 (19)
IDH	Pig heart (Boehringer)	isocitrate & [2-^{2}H]isocitrate	$NADP^+$, Mg^{2+}	7.04	0.76	+316	Ramachandran et al., 1974 (21)
IDH	Pig heart (Sigma)	isocitrate & [2-^{2}H]isocitrate	$NADP^+$, Mg^{2+}	5.5	0.95 ± 0.3	+53	O'Leary and Limburg, 1977 (22)
IDH	Pig heart (Sigma)	isocitrate & [2-^{2}H]isocitrate	$NADP^+$, Mg^{2+}	7.5	0.76 ± 0.12	+316	O'Leary and Limburg, 1977 (22)
IDH	Pig heart (Sigma)	isocitrate & [2-^{2}H]isocitrate	$NADP^+$, Mg^{2+}	8.5	1.07 ± 0.17	−65	O'Leary and Limburg, 1977 (22)
IDH	Pig heart (Sigma)	isocitrate & [2-^{2}H]isocitrate	$NADP^+$, Ni^{2+}	7.5	1.11 ± 0.14	−99	O'Leary and Limburg, 1977 (22)
ALDH	*Vibrio harveyi* (expressed in *Escherichia coli*)	acetaldehyde & [1-^{2}H]acetaldehyde	$NADP^+$, K^+	8	3.19	−687	Vedadi and Meighen, 1997 (23)
ALDH	*Vibrio harveyi* (expressed in *Escherichia coli*)	(saturating) acetaldehyde & [1-^{2}H]acetaldehyde	$NADP^+$(variable), K^+	8	1.227	−185	Vedadi and Meighen, 1997 (23)

[a] The primary deuterium isotope effect on enzyme rate constants (KIE) is $^2(V/K) = (V_{max}/K_m)^{1H}/(V_{max}/K_m)^{2H}$, unity indicates no fractionation and values >1 indicate the reaction is faster with ^{1}H.

[b] ^{2}H-enrichment factor calculated as (1/KIE – 1) x 1000.

Table S2. Statistical analyses of relationships between fatty acid/water ^{2}H-fractionations for glycerol and glucose fed strain EXF-4126 in chemostats with physiological and isotopic parameters. See **Fig. S9**, ***Data S3*** for details.

Ordinate	Abscissa	n	Pearson *r*	Pearson p_{val}	York Intercept (σ)	York Slope (σ)	York p_{val}
glycerol & glucose $^{2}\varepsilon_{fattyacid/water}$ (‰)	$^{2}\varepsilon_{16:1/16:0}$ (‰)	6	−0.88	0.02	−921 (50)	−8 (0)	1.00
	growth rate (d^{-1})	6	−0.09	0.87	−9 (17)	11 (22)	1.00
	% cytosolic IDH to NADPH	6	1.00	0.00	−2 (0)	20 (2)	0.03
	% total IDH to NADPH	6	0.98	0.00	−8 (1)	30 (5)	0.08
	C/N	6	−0.59	0.22	14 (3)	−1 (0)	1.00
	% unsaturated fatty acids	6	−0.26	0.62	−4 (6)	4 (7)	0.99
	relative abundance lipid (µg fatty acid mg biomass^{-1})	6	−0.77	0.07	1433 (434)	−24 (7)	0.91
	relative abundance lipid^{-1} (mg biomass µg fatty acid^{-1})	6	0.85	0.03	−14 (4)	887 (299)	0.99

SI Methods

(1) Yeast chemostats

Nitrogen sources for culture media were ammonium sulfate (A-4418 lot 100K5442, Sigma-Aldrich, St Louis, MO, USA) and amino acids (R459932 lot 165196, Remel Inc., San Diego, CA, USA). Media was prepared in 5 or 10 L batches, MilliQ water was autoclaved and media components added through a 0.2 µm Rapid-Flow bottle top filter (#595-4520, Nalgene, Thermo Fisher Scientific, Waltham, MA, USA). The media was unbuffered (starting pH = 4, steady state pH ranged from 2.96 to 3.34).

For each chemostat, prior to turning on the pumps to initiate steady-state conditions, 1–3 samples were taken that represent late exponential/early stationary batch conditions in the bioreactors; pumps were turned on in early stationary phase. Once in steady state the 2% glucose and 2% glycerol (strain EXF-4126) chemostats were sampled multiple times at three growth rates ranging from 0.55 to 2.69 d^{-1} and the 0.75% glucose or galactose (strain FY4) were sampled at three growth rates ranging from 1.18 to 6.51 d^{-1}. To sample bioreactors for biomass and OD a syringe was used to clear and flush sample port dead space; a maximum of 50 ml was only taken ~every other day to avoid altering culture volume and growth conditions; samples for enzyme, protein concentration, and NADPH assays were either collected by syringe and immediately put on ice or passively collected from chemostat overflow into a sterile tube on ice and immediately processed or frozen (−80 °C, less than 1 week). To obtain sufficient biomass for lipid isotope analysis, 0.5 to 1 L samples were collected by allowing the chemostat overflow to fill pre-combusted bottles sitting on ice. Samples were either filtered (47 mm pre-combusted Whatman GF/C), folded, and wrapped in pre-combusted foil (strain FY4), or spun down and transferred to pre-combusted glass vials (strain EXF-4126), samples for lipid isotope analysis were stored at −20 °C until analysis.

Concentrations of bioavailable nitrogen in supernatant were determined at the Moss Landing Marine Labs Anlytical Nutrient Lab via a Lachat Quickchem 8000 Flow Injection Analyzer. Concentrations of ethanol in supernatant were determined using an ethanol assay kit (product code K-ETOH, Megazyme, Brey, Ireland). Ethanol in carbohydrate-fed cultures was two to three times greater than glycerol-fed cultures demonstrating fermentative activity in carbohydrate-fed cultures (**Fig. S5**)**.** Dissolved oxygen levels (measured in the 2% glucose or 2% glycerol (strain EXF-4126) cultures only) were monitored to ensure oxygen was not limiting and remained high and constant throughout the chemostat. For strain EXF-4126 we noticed oxidative reductive potential (ORP) levels fluctuating greatly with ambient light levels. Therefore, we only considered chemostats to be in steady state after modifying ambient lab light levels to remain low and constant, allowing ORP to stay constant at each growth rate. Given the long length of time required for achieving steady-state conditions at the slowest growth rates used for strain EXF-4126 (and solving the light issue) we verified there were no mutations that could impact growth rate by plating cells from each vessel at the end of the chemostats and a fresh inoculate from EXF-4126 freezer stock, and growing these three "sub strains" side by side; we found no growth rate differences between the three samples. Periodically during chemostats, culture purity was confirmed by plating ~0.25 ml of culture onto agar with rich media and 2% glucose which remained clear of non-yeast colonies.

(2) Fatty acid hydrogen isotopic analyses

Fatty acid identification and quantification were achieved using a Trace 1310 gas chromatograph oven equipped with a flame ionization detector (FID) and an ISQ QD mass spectrometer (MS) (Thermo Fisher Scientific, Waltham, MA, USA) and two 30 m, 0.25 mm diameter, 0.25 µm thick DB-5 columns (Agilent Tech., Santa Clara, CA, USA) fitted to the back inlet and the FID and the front inlet to the MS; 5**α**-cholestane added to 5% aliquots was used as a quantification standard. Instrument settings included 320 °C split/splitless inlets operated in splitless mode with a constant flow of He carrier gas at 1.1 ml min^{-1}; oven temperature started at 90 °C for 1 min; ramped to 120 °C at 20 °C min^{-1}; ramped to 320 °C at 5 °C min^{-1}, ending with a 13 min hold.

Fatty acid hydrogen isotope ratios were measured by gas chromatography-pyrolysis-isotope ratio mass spectrometry using a Trace 1310 gas chromatograph-GC Isolink II coupled to a 253 Plus isotope ratio mass spectrometer via a ConFlo IV (Thermo Fisher Scientific, Waltham, MA, USA) in the Dept of Geological Sciences, University of Colorado, Boulder.

A 60 m by 0.25 mm and 0.25 µm film thickness DB-1 GC column was used for yeast samples (Agilent Tech., Santa Clara, CA, USA); a ZB-5HT 30 m by 0.25 mm and 0.25 µm film thickness GC column was used for mammal cell samples (Phenomenex Zebron, Torrance, CA, USA). A programmable temperature inlet in splitless mode had a starting temperature of 250 °C with a 0.1 min injection phase, ramped to 300 °C at 5 °C min^{-1} for a 0.1 min evaporation phase, ramped to 400 at 8 °C min^{-1} for 1 min transfer phase followed by a 10 min cleaning phase at 350 °C, all with a constant helium carrier flow of 1.2 ml min^{-1}. The oven temperature started at 80 °C with a 2 min hold, ramped to 130 °C at 20 °C min^{-1}, ramped to 320 °C at 5 °C min^{-1} with a final 12 min hold. H3+ factors were monitored daily and ranged from 8.28 to 7.29 during the 1.5 year timespan that hydrogen isotope measurements for this study took place. The $^2H/^1H$ values, reported in δ^2H notation in permil (‰), were evaluated to hydrogen reference gas pulses at the beginning and end of each run, then externally corrected to A7 and F8 isotope standard mixes (Dr. Arndt Schimmelmann, Indiana University, available at: https://hcnisotopes.earth.indiana.edu/reference-materials/index.html). Due to the higher δ^2H values in the glycerol grown samples, the glycerol-fed cultures used the following additional standards to bracket the analytical range of the samples: C16E (+275.6 ‰), C16P (+449.3 ‰), C20P (+191.9‰), C20B (+1.5‰) (Dr. Arndt Schimmelmann, Indiana University). These were injected throughout the sequence in separate injections from the A7 and F8 mixes to avoid memory effects that occur when a light analyte follows an enriched analyte in the same injection. In addition to samples, a phthalic acid isotope standard (−95.5 ± 2.2‰, Dr. Arndt Schimmelmann, Indiana University) was methylated with the same batch of MeOH used for samples to obtain the isotope composition of the derivatizing H. A mass balance calculation corrected all measured FAMES for the added methyl group H and errors on reported values were calculated by propagating errors from analytical uncertainty of samples (standard deviations if 3 injections, differences if 2 injections) and phthalic acid isotope standard.

(3) Substrate isotopic analyses

Substrate hydrogen isotope composition was determined by two methods: substrate acetylation and equilibration (24). In method 1, we prepared acetylated derivatives of substrates (glucose, galactose, glycerol) using acetic anhydride of known isotopic composition (−133.2 ± 2.1‰, Arndt Schimmelmann, Indiana University) and pyridine in vials capped under a stream of N_2 gas and heating to 50 °C for 1 hr. The derivatization created glucose-acetate, galactose-acetate, and glycerol-acetate which were analyzed via GC-P-IRMS. The preparation and measurement of sugar- and sugar alcohol-acetate substrates was performed at both University of Colorado, Boulder and University of Basel using subsamples from identical substrate jars including glycerol (Thermo Scientific Arco part number 410980100, lot A0388846), glucose (Sigma part number G8270 lot SLBV7620), and galactose (Sigma part number G0625 lot SLBT4248). The second method used an equilibration experiment following previously reported procedures (24), performed at Northwestern University. The average of 3 to 4 δ^2H values of substrate H using the two methods measured by three institutions are reported and errors are represented by the standard deviations between those values: $\delta^2H_{glycerol}$ = −45±5‰, $\delta^2H_{glucose}$= 8±10 ‰, and $\delta^2H_{galactose}$ = 40±20‰.

(4) Biomass elemental analyses

Samples for elemental analysis of strain FY4 were collected at similar time points as samples for lipid isotope analysis onto pre-combusted 25 mm GF/D (nominal pore size 1.2 *µ*m, Whatman), folded in half (loaded side in), and stored in combusted aluminum foil at −20 °C until analysis. Samples from strain EXF-4126 were pellets collected during steady state in addition to sub-aliquots from the identical freeze-dried biomass fraction also used for lipid isotope analysis. Frozen/wet

samples of biomass and substrate carbon were oven dried overnight (60 °C) and either packed (filters) or weighed (dried biomass, substrate) into tin capsules (9x10 mm, Elemental Microanalysis and Costech) prior to elemental analyses of total C and N and their isotopes.

(5) Enzyme assays

Cell pellets for enzyme assays were disrupted with a pipette by adding 1 ml cold extraction buffer then transferred to cold pre-combusted 2 ml flat-bottomed glass vials with ~0.3 ml of disruption beads (pre-combusted and rinsed 3 times with extraction buffer solution; extraction buffer identical to wash buffer but without protease inhibitor tabs). To break cells, samples were vortexed for 30 s followed by freezing in ice bath for 30 s, repeated three times. Material was transferred to a low-binding mini centrifuge tube on ice and spun down (2 °C, 3 min, max rpm); the top debris-free layer was transferred to a new mini centrifuge tube on ice and diluted 1:1 with cold extraction buffer, this was spun down again just prior to loading wells using the topmost layer. NADPH production by G6PDH+6PGDH (25), 6PGDH, IDH, and ALDH was simultaneously measured in a Costar 96 flat bottom plate plus lid by aliquoting 45 µl sample extracts into triplicate wells for each target enzyme with 45 µl freshly prepared 2.22 mM $NADP^+$, after 30 s of orbital shaking (frequency 282 cpm (3 mm) before and after a 10 min delay at 30 °C, 10 µl of substrate was added to sample wells (at final concentrations 10 mM for isocitrate, 5 mM for acetaldehyde, and 3.3 mM for 6-phosphogluconate and glucose 6-phosphate) followed by a programmed kinetic procedure of 30 s orbital shaking plus a 340 nM reading every 42 s for 40 min. Wavelength reads were blank corrected (using the average of 3 to 6 nearby wells containing 45 ul buffer instead of sample) and all wells were pathlength corrected. In addition to samples, sample-free control wells were monitored for each substrate type and control well Vmax (maximum slope of the curve) values were subtracted from sample well Vmax values for a control-corrected sample Vmax value. To obtain Vmax values for G6PDH, the Vmax results from control-corrected 6PGDH wells were subtracted from control-corrected G6PDH+6PGDH wells. Triplicate 25 µl aliquots of extract from the same samples were used to determine protein concentrations using a BCA Protein Assay Kit (Thermo Fisher Scientific, Waltham, MA, USA). All reagents were 0.2 µm filter sterilized. All assays were performed on a BioTek Synergy HTX multi-mode plate reader (BioTek, Winooski, Vermont, USA). Sample control-corrected Vmax slopes were normalized to BCA protein concentrations, pathlength (these averaged ~0.25 cm per well depth), and the extraction coefficient of NADPH at 340 nm of 6.22 liter NADPH $mmol^{-1}$ cm^{-1} (26, 27).

Calculations of relative contributions to NADPH based on protein activity data assume 1) similar protein extraction efficiencies and for cytosolic IDH 2) only mitochondrial IDH is active for glucose metabolism such that the cytosolic contribution (% cyto IDH) in glycerol metabolism is estimated by correcting for the estimated mitochondrial component.

SI Discussion

(1) Possible ^{2}H-enrichment of substrates supplying NADPH enzymes in glycerol grown cells

It is possible that the substrates feeding all four enzymes are likely heavier in ^{2}H in the glycerol respiring cells than sugar fermenting cells because: 1) the reactions in the TCA cycle fractionate hydrogen, producing ^{2}H-enriched isocitrate (see discussion in (6)); 2) acetaldehyde-H originates from cell water which can become isotopically distinct from the growth medium (28, 29), and in natural abundance waters can be heavier than medium (30); and 3) hexose precursors for oxPPP enzymes (G6PDH and 6PGDH) supplied by gluconeogenesis can pick up hydrogen from water (via triosephosphate isomerase mediated interconversion of dihydroxyacetone phosphate (DHAP) and glyceraldehyde-3-phosphate (GAP)) and have the potential to be additionally ^{2}H-enriched if gluconeogenesis enzymes in yeast have inverse deuterium isotope effects (**Fig. 1** and **Fig. S1**). Hayes (31) notes that the exchange of carbon-bound H on carbohydrate with water has an inverse isotope effect ($^2\alpha_{carbohydrate/water} > 1$; $^2\varepsilon_{carbohydrate/water} > 0$) favoring ^{2}H-enrichment in carbohydrate. Thus, NADPH from gluconeogenesis may also be ^{2}H-enriched due to the inheritance of isotopic signals from ^{2}H-enriched hexoses that result from isomerize-catalyzed equilibration reactions with water

which have an inverse isotope effect. Such exchanges have been associated with a ~ 100‰ ^{2}H-enrichment of plant cellulose (31, 32). Equilibrium isotope effects cannot be the primary driver of the much larger (~ 500‰) ^{2}H-enrichment observed in glycerol grown cell lipids. This is consistent with the IDH activity as the primary control on lipid ^{2}H-enrichment under this condition.

(2) Variable ^{2}H-fractionation between unsaturated and saturated fatty acids

We observed variable ^{2}H-depletions in the ^{2}H-fractionation between palmitoleic acid (one unsaturation) and fully saturated palmitic acid ($^{2}\varepsilon_{16:1/16:0}$ between ~ −50‰ and −150‰, **Fig. S11** and **Fig. S12**), especially in glycerol-fed EXF-2146 (**Fig. 2*A*, Fig. S11** and **Fig. S12**). Desaturase enzymes with normal dKIE produce unsaturated fatty acids from their saturated counterparts (33). Chikaraishi et al. (34) proposed that the size of unsaturated lipid flux from the saturated pool could explain the large ^{2}H-depletions measured in the most abundant fatty acids of macroalgae (33)**.** Regressions of $^{2}\varepsilon_{16:1/16:0}$ against the relative abundance of unsaturated fatty acids in 16 carbon fatty acids (% unsaturation, **Fig. S11**) for glucose grown cells support this interpretation (Pearson p_{val} = 0.059, York p_{val} = 0.13, **Fig. S11**), but $^{2}\varepsilon_{16:1/16:0}$ values for other conditions (e.g., EXF-2146 on glycerol, FY4 on glucose, galactose, **Fig. S11** and **Fig. S12*A***) and other organisms do not show consistent trends with fatty acid relative abundance. Only chemostats of strain EXF-4126 grown on 2% substrates had a linear relationship between $^{2}\varepsilon_{16:1/16:0}$ and $^{2}\varepsilon_{lipid/water}$ (**Fig. S12*B***). The controls on fractionation between fatty acid pools merit additional research.

(3) Biomass ^{13}C enrichments in glycerol-respiring cultures: Possible autophagy

The results showing higher biosynthetic costs (**Fig. 3, Fig. S4** and **Fig. S6**) and biomass/substrate ^{13}C isotope fractionations (**Fig. 2*A*** and **Fig. S13**) for glycerol respiration compared to carbohydrate fermentation suggest that glycerol-fed cells could recycle biomass via general autophagy, β-oxidation in the peroxisome, or μ-lipophagy, which occur under acute glucose starvation (35). In yeast, autophagy is a normal housekeeping process that occurs at basal levels, increases with nutrient and carbon limitation (36, 37), and is required for mitochondrial function on non-fermentable substrates like glycerol (38). The observed increased activity of aldehyde dehydrogenase in the glycerol-fed chemostat with growth rate (**Fig. 3*C***) may signal export of fatty acids from cells or their consumption for energy thus requiring additional acetate to supply acetyl-CoA for *de novo* lipid synthesis. Such a process could help explain why lipid unsaturation and concentration does not vary with growth rate in glycerol-respiring cells like they do in glucose-fermenting cells (**Fig. S8*A*–*C***) and why lipid concentrations are lower for glycerol respiration compared to glucose fermentation (**Fig. S8*A*** and ***B***). Notably, ^{13}C-enrichments of glycerol culture biomass were only observed once N-limited steady state conditions had established in chemostats (**Fig. S13**), suggesting a relationship between nitrogen availability, $^{13}C_{biomass}$, and inferred autophagy.

(4) Miscellaneous impacts on lipid/water ^{2}H-fractionation

In addition to $NADP^{+}$ reducing enzyme activity, NADPH ^{2}H in fast growing glycerol cultures may be sensitive to NADPH consumption/supply. Variations in NADPH demand have been inferred for antioxidant defense between respiring and fermenting yeast (40–42). The higher reductant costs of glycerol growth (**Fig. 3*E*** and **Fig. S4*A***) could thus reflect increased oxidative stress (43–45) and/or enhanced lipid recycling for aerobic respiration relative to aerobic fermentation (see ***SI Discussion 3***). These demands may have been satisfied by supplementing relatively ^{2}H-depleted NAPDH from oxPPP pathways to the NAPDH pool, helping explain strong lipid ^{2}H decreases with growth rate in glycerol but not glucose fed cells.

Our experiments revealed a high sensitivity of yeast $^{2}\varepsilon_{fattyacid/water}$ to NADPH production by IDH (~30 + 5‰ per 1 p.p. NAPDH from IDH, **SI Table 2**). Although shifts in biomass composition observed in glucose cultures did not significantly affect IDH control of $^{2}\varepsilon_{fattyacid/water}$ (**Fig. 4*A*)**, much larger changes in cellular composition (**Fig. 4*B***) could alter quantitative relationships between IDH and $^{2}\varepsilon_{fattyacid/water}$. In other words, NADPH sinks could alter the sensitivity of $^{2}\varepsilon_{fattyacid/water}$ to NAPDH source

(slope of $^2\varepsilon_{fattyacid/water}$ line vs IDH contributed NADPH) if they were sufficiently large. In general, the sensitivity of $^2\varepsilon_{fattyacid/water}$ to NAPDH source could be affected by enzyme-mediated hydrogen atom exchange between NAPDH and water (46, 47) and NADH (12), mechanisms also discussed in ref (1). These can have extremely large kinetic isotope effects (12, 48) and their influence should be modulated by enzyme levels and metabolite turnover rates. Cellular compartmentalization that decouples lipid biosynthesis from IDH activity in another cellular location may also shift $^2\varepsilon_{lipid/water}$ - NAPDH source relationships in different eukaryotes. Finally, changes in lipid biosynthetic patterns and poorly known biosynthetic pathways for NADPH and lipids should also be considered.

(5) Growth rate impacts on lipid/water ^{2}H-fractionation in other microorganisms

Yeast data inform the mechanisms of growth rate dependency for ^{2}H-fractionations measured in marine phytoplankton lipids (4, 39), archaeal lipids (14), and bacterial amino acids (15) (**Fig. S14**). Fatty acid/water ^{2}H-fractionation from the haptophyte *Emiliania huxleyi* responds strongly to growth rate as in glycerol-grown yeast. Brassicasterol and alkenones from *E. huxleyi* and sterols and fatty acids from *Thalassiosira pseudonana* are less sensitive to growth rate, as in glucose-grown yeast, while archaeal GDGTs and most amino acids from *Escherichia coli* show little to no response to growth rate. The larger variations in $^2\varepsilon_{lipid/water}$ with growth rate likely originate from NADPH source shifts, while smaller variations may indicate NADPH demand changes related to cellular composition. Alternatively, they could reflect very small source shifts (or muting of source signals via the mechanisms described above), or some combination of these.

(6) Interpretation of murine lipid/water ^{2}H-fractionation

NADPH fluxes for *de novo* lipid synthesis were determined by MFA in the same healthy murine hepatocytes used in this study and in the HepG2 human hepatocarcinoma-lineage under the conditions employed here (49). Notably, HepG2 cells relied heavily on oxPPP (>80% cytosolic NADPH) for *de novo* lipid biosynthesis, while healthy murine hepatocytes instead obtained NAPDH from cytosolic IDH and malic enzyme flux in the TCA cycle (~40%), cytosolic serine catabolism (>50%), and one-carbon metabolism (~5%) (49). These results point to IDH activity as the source of the observed lipid ^{2}H-enrichment in respiring murine hepatocytes, as we found for yeast. Compared to yeast results, the lower sensitivity of hepatocyte lipid ^{2}H-fractionation to differences in IDH-derived NAPDH likely reflect several unconstrained parameters. These include (i) the fraction of measured lipids derived from *de novo* lipid biosynthesis during the 24 hr plate culture experiment vs. carried over from living mice (healthy hepatocytes, in which ~50–90% lipids derive directly from diet (49) or the maintenance medium; (ii) differences in NADPH cycling between human hepatocarcinoma (49) and its murine counterpart (50, 51) used here; (*iii*) flavin enzyme-mediated exchange of NADPH-hydrogen with water active in the cells along with H exchange between NADH and NADPH by transhydrogenase in mammalian cells (46) but not yeast (52); (*iv*) the direct influence of substrate ^{2}H-isotopic composition on lipids (e.g., X_s, the fraction of lipid H that is substrate H (6)); as well as (v) the dKIE of NADPH produced by serine catabolism (53).

SI REFERENCES

1. T. Xiao, A. Khan, Y. Shen, L. Chen, J. D. Rabinowitz, Glucose feeds the tricarboxylic acid cycle via excreted ethanol in fermenting yeast. *Nat. Chem. Biol.* **18**, 1380–1387 (2022).
2. D. York, N. M. Evensen, M. L. Martínez, J. De Basabe Delgado, Unified equations for the slope, intercept, and standard errors of the best straight line. *Am. J. Phys.* **72**, 367–375 (2004).
3. A. E. Maloney, A. L. C. Shinneman, K. Hemeon, J. P. Sachs, Exploring lipid ^{2}H/^{1}H fractionation mechanisms in response to salinity with continuous cultures of the diatom *Thalassiosira pseudonana*. *Org. Geochem.* **101**, 154–165 (2016).
4. J. P. Sachs, O. E. Kawka, The influence of growth rate on ^{2}H/^{1}H fractionation in continuous cultures of the coccolithophorid *Emiliania huxleyi* and the diatom *Thalassiosira pseudonana*. *PLoS One* **10**, e0141643 (2015).
5. S. M. Heinzelmann, *et al.*, Impact of metabolism and growth phase on the hydrogen isotopic composition of microbial fatty acids. *Front. Microbiol.* **6**, 1–11 (2015).

6. X. Zhang, A. L. Gillespie, A. L. Sessions, Large D/H variations in bacterial lipids reflect central metabolic pathways. *Proc. Natl. Acad. Sci. U. S. A.* **106**, 12580–6 (2009).
7. B. J. Campbell, C. Li, A. L. Sessions, D. L. Valentine, Hydrogen isotopic fractionation in lipid biosynthesis by H2-consuming *Desulfobacterium autotrophicum*. *Geochim. Cosmochim. Acta* **73**, 2744–2757 (2009).
8. J. P. Sachs, A. E. Maloney, J. Gregersen, Effect of light on $^{2}H/^{1}H$ fractionation in lipids from continuous cultures of the diatom *Thalassiosira pseudonana*. *Geochim. Cosmochim. Acta* **209**, 204–215 (2017).
9. A. L. Sessions, L. L. Jahnke, A. Schimmelmann, J. M. Hayes, Hydrogen isotope fractionation in lipids of the methane-oxidizing bacterium *Methylococcus capsulatus*. *Geochim. Cosmochim. Acta* **66**, 3955–3969 (2002).
10. R. S. Wijker, A. L. Sessions, T. Fuhrer, M. Phan, $^{2}H/^{1}H$ variation in microbial lipids is controlled by NADPH metabolism. *Proc. Natl. Acad. Sci.* **116**, 1–10 (2019).
11. M. R. Osburn, K. S. Dawson, M. L. Fogel, A. L. Sessions, Fractionation of hydrogen isotopes by sulfate- and nitrate-reducing bacteria. *Front. Microbiol.* **7**, 1–16 (2016).
12. W. D. Leavitt, T. M. Flynn, M. K. Suess, A. S. Bradley, Transhydrogenase and growth substrate influence lipid hydrogen isotope ratios in *Desulfovibrio alaskensis* G20. *Front. Microbiol.* **7**, 1–14 (2016).
13. W. D. Leavitt, S. S. Venceslau, I. A. C. Pereira, D. T. Johnston, A. S. Bradley, Fractionation of sulfur and hydrogen isotopes in *Desulfovibrio vulgaris* with perturbed DsrC expression. *FEMS Microbiol. Lett.* **363**, 1–8 (2016).
14. W. D. Leavitt, *et al.*, Controls on the hydrogen isotope composition of tetraether lipids in a marine thaumarchaeon (2022).
15. D. A. Smith, B. J. Nakamoto, M. K. Suess, M. L. Fogel, Central metabolism and growth rate impacts on hydrogen and carbon isotope fractionation during amino acid synthesis in *E. coli*. *Front. Microbiol.* **13**, 1–15 (2022).
16. J. D. Hermes, C. A. Roeske, M. H. O'Leary, W. W. Cleland, Use of multiple isotope effects to determine enzyme mechanisms and intrinsic isotope effects. Malic enzyme and glucose 6-phosphate dehydrogenase. *Biochemistry* **21**, 5106–5114 (1982).
17. A. R. Rendina, J. D. Hermes, W. W. Cleland, Use of multiple isotope effects to study the mechanism of 6-phosphogluconate dehydrogenase. *Biochemistry* **23**, 6257–6262 (1984).
18. C. B. Grissom, W. W. Cleland, Isotope effect studies of the chemical mechanism of pig heart NADP isocitrate dehydrogenase. *Biochemistry* **27**, 2934–2943 (1988).
19. P. F. Cook, W. W. Cleland, pH variation of isotope effects in enzyme-catalyzed reactions. 1. Isotope- and pH-dependent steps the same. *Biochemistry* **20**, 1797–1805 (1981).
20. M. H. O'Leary, Multiple isotope effects on enzyme-catalyzed reactions. *Annu. Rev. Biochem.* **58**, 377–401 (1989).
21. N. Ramachandran, M. Durbano, R. F. Colman, Kinetic isotope effects in the NAD- and NADP-specific isocitrate dehydogneases of pig heart. *FEBS Lett.* **49**, 129–133 (1974).
22. M. H. O'Leary, J. A. Limburg, Isotope effect studies of the role of the metal ions in isocitrate dehydrogenase. *Biochemistry* **16**, 1129–1135 (1977).
23. M. Vedadi, E. Meighen, Critical glutamic acid residues affecting the mechanism and nucleotide specificity of *Vibrio harveyi* aldehyde dehydrogenase. *Eur. J. Biochem.* **246**, 698–704 (1997).
24. M. M. Holloway-Phillips, *et al.*, Species variation in the hydrogen isotope composition of leaf cellulose is mostly driven by isotopic variation in leaf sucrose. *Plant Cell Environ.* **45**, 2636–2651 (2022).
25. W. N. Tian, *et al.*, Importance of glucose-6-phosphate dehydrogenase activity for cell growth. *J. Biol. Chem.* **273**, 10609–10617 (1998).
26. H. U. Bergmeyer, New value for the molar extinction coefficients of NADH and NADPH for use in the routine laboratory. *Medizinische Lab.* **30**, 57–59 (1977).
27. D. S. Sigman, Interactions of substrates, inhibitors, and coenzymes at the active site of horse liver alcohol dehydrogenase. *J. Biol. Chem.* **242**, 3815–3824 (1967).
28. H. W. Kreuzer, *et al.*, Detection of metabolic fluxes of O and H atoms into intracellular water in mammalian cells. *PLoS One* **7**, e39685 (2012).
29. H. W. Kreuzer-Martin, J. R. Ehleringer, E. L. Hegg, Oxygen isotopes indicate most intracellular water in log-phase *Escherichia coli* is derived from metabolism. *Proc. Natl. Acad. Sci.* **102**, 17337–41 (2005).
30. H. W. Kreuzer-Martin, M. J. Lott, J. R. Ehleringer, E. L. Hegg, Metabolic processes account for the majority of the intracellular water in log-phase *Escherichia coli* cells as revealed by hydrogen isotopes. *Biochemistry* **45**, 13622–13630 (2006).
31. J. M. Hayes, Fractionation of carbon and hydrogen isotopes in biosynthetic processes. *Reveiws Mineral. Geochemistry* **43**, 225–227 (2001).
32. Y. Luo, L. Sternberg, Deuterium heterogeneity in starch and cellulose nitrate of CAM and C3 plants. *Phytochemistry* **30**, 1095–1098 (1991).
33. P. H. Buist, B. Behrouzian, Use of deuterium kinetic isotope effects to probe the cryptoregiochemistry of Δ9 desaturation. *J. Am. Chem. Soc.* **118**, 6295–6296 (1996).
34. Y. Chikaraishi, Y. Suzuki, H. Naraoka, Hydrogen isotopic fractionations during desaturation and elongation associated with polyunsaturated fatty acid biosynthesis in marine macroalgae. *Phytochemistry* **65**, 2293–2300 (2004).
35. C. A. Weber, *et al.*, β-Oxidation and autophagy are critical energy providers during acute glucose depletion in

Saccharomyces cerevisiae. *Proc. Natl. Acad. Sci.* **117**, 12239–12248 (2020).
36. R. Iwama, Y. Ohsumi, Analysis of autophagy activated during changes in carbon source availability in yeast cells. *J. Biol. Chem.* **294**, 5590–5603 (2019).
37. K. Liu, B. M. Sutter, B. P. Tu, Autophagy sustains glutamate and aspartate synthesis in *Saccharomyces cerevisiae* during nitrogen starvation. *Nat. Commun.* **12** (2021).
38. A. I. May, M. Prescott, Y. Ohsumi, Autophagy facilitates adaptation of budding yeast to respiratory growth by recycling serine for one-carbon metabolism. *Nat. Commun.* **11**, 1–14 (2020).
39. Z. Zhang, J. P. Sachs, A. Marchetti, Hydrogen isotope fractionation in freshwater and marine algae: II. Temperature and nitrogen limited growth rate effects. *Org. Geochem.* **40**, 428–439 (2009).
40. K. I. Minard, L. McAlister-Henn, Antioxidant function of cytosolic sources of NADPH in yeast. *Free Radic. Biol. Med.* **31**, 832–843 (2001).
41. K. I. Minard, C. A. Carroll, S. T. Weintraub, L. Mc-Alister-Henn, Changes in disulfide bond content of proteins in a yeast strain lacking major sources of NADPH. *Free Radic. Biol. Med.* **42**, 106–117 (2007).
42. K. I. Minard, L. McAlister-Henn, Sources of NADPH in yeast vary with carbon source. *J. Biol. Chem.* **280**, 39890–39896 (2005).
43. K. H. Slekar, D. J. Kosman, V. C. Culotta, The yeast copper/zinc superoxide dismutase and the pentose phosphate pathway play overlapping roles in oxidative stress protection. *J. Biol. Chem.* **271**, 28831–28836 (1996).
44. R. Maslanka, R. Zadrag-Tecza, M. Kwolek-Mirek, Linkage between carbon metabolism, redox status and cellular physiology in the yeast *Saccharomyces cerevisiae* devoid of SOD1 or SOD2 gene. *Genes (Basel).* **11**, 1–19 (2020).
45. E. Macierzyńska, A. Grzelak, G. Bartosz, The effect of growth medium on the antioxidant defense of Saccharomyces cerevisiae. *Cell. Mol. Biol. Lett.* **12**, 448–456 (2007).
46. Z. Zhang, L. Chen, L. Liu, X. Su, J. D. Rabinowitz, Chemical basis for deuterium labeling of fat and NADPH. *J. Am. Chem. Soc.* **139**, 14368–14371 (2017).
47. K. Saito, K. Akihiko, O. Shigenobu, S. Yousuke, Y. Tamio, Incorporation of hydrogen atoms from deuterated water and stereospecifically deuterium-labeled nicotinamide nucleotides into fatty acids with the *Escherichia coli* fatty acid synthetase system. *Biochim. Biophys. Acta* **618**, 202–213 (1980).
48. H.-L. Schmidt, R. A. Werner, W. Eisenreich, Systematics of ^{2}H patterns in natural compounds and its importance for the elucidation of biosynthetic pathways. *Phytochem. Rev.* **2**, 61–85 (2003).
49. Z. Zhang, *et al.*, Serine catabolism generates liver NADPH and supports hepatic lipogenesis. *Nat. Metab.* **3**, 1608–1620 (2021).
50. G. J. Darlington, H. P. Bernhard, R. A. Miller, F. H. Ruddle, Expression of liver phenotypes in cultured mouse hepatoma cells. *J. Natl. Cancer Inst.* **64**, 809–819 (1980).
51. S. Cassim, V. A. Raymond, L. Dehbidi-Assadzadeh, P. Lapierre, M. Bilodeau, Metabolic reprogramming enables hepatocarcinoma cells to efficiently adapt and survive to a nutrient-restricted microenvironment. *Cell Cycle* **17**, 903–916 (2018).
52. P. M. Bruinenberg, The NADP(H) redox couple in yeast metabolism. *Antonie Van Leeuwenhoek* **52**, 411–429 (1986).
53. M. A. Vanoni, R. G. Matthews, Kinetic isotope effects on the oxidation of reduced nicotinamide adenine dinucleotide phosphate by the flavoprotein methylenetetrahydrofolate reductase. *Biochemistry* **23**, 5272–5279 (1984).